nature materials

Article

https://doi.org/10.1038/s41563-024-01987-w

A metastable pentagonal 2D material synthesized by symmetry-driven epitaxy

Received: 5 October 2022

Accepted: 1 August 2024

Lina Liu[1,2,3,9], **Yujin Ji**[4,9], **Marco Bianchi**[5], **Saban M. Hus**[6], **Zheshen Li**[7], **Richard Balog**[3], **Jill A. Miwa**[5], **Philip Hofmann**[5], **An-Ping Li**[6], **Dmitry Y. Zemlyanov**[2] ✉, **Youyong Li**[4] ✉ & **Yong P. Chen**[1,2,3,8] ✉

Most two-dimensional (2D) materials experimentally studied so far have hexagons as their building blocks. Only a few exceptions, such as $PdSe_2$, are lower in energy in pentagonal phases and exhibit pentagons as building blocks. Although theory has predicted a large number of pentagonal 2D materials, many of these are metastable and their experimental realization is difficult. Here we report the successful synthesis of a metastable pentagonal 2D material, monolayer pentagonal $PdTe_2$, by symmetry-driven epitaxy. Scanning tunnelling microscopy and complementary spectroscopy measurements are used to characterize this material, which demonstrates well-ordered low-symmetry atomic arrangements and is stabilized by lattice matching with the underlying Pd(100) substrate. Theoretical calculations, along with angle-resolved photoemission spectroscopy, reveal monolayer pentagonal $PdTe_2$ to be a semiconductor with an indirect bandgap of 1.05 eV. Our work opens an avenue for the synthesis of pentagon-based 2D materials and gives opportunities to explore their applications such as multifunctional nanoelectronics.

Since the prediction several years ago of the first pentagonal two-dimensional (2D) materials, namely, pentagonal graphene[1] and noble metal dichalcogenides[2], research interest has been growing in this subgroup of 2D materials due to their unique properties and potential applications in nanoelectronics, optoelectronics and thermoelectrics[3,4]. Unlike the much more studied hexagon-based 2D materials, the building blocks of pentagonal 2D materials are pentagons. Due to the well-known pentagonal tiling rule, according to which regular pentagons cannot tile a plane, pentagonal 2D materials tend to form puckered layers. Such a puckered pentagon-based structure presents low crystallographic symmetry, leading to an orthorhombic crystal structure with rectangular unit cells[5]. The low crystallographic symmetry introduces large in-plane anisotropy and low thermal conductivity, making them promising candidate materials for future anisotropic electronics and thermoelectrics[6–10]. The puckered layers in pentagonal 2D materials also induce renormalization of bond lengths and angles, resulting in decreased layer thickness and increased layer flexibility[11]. This makes pentagonal transition metal dichalcogenide (TMDC) monolayers ~40–50% thinner than hexagonal TMDC monolayers[11] and could facilitate applications in flexible devices and wearable electronics. Furthermore, many other fascinating properties have been predicted for pentagonal 2D materials, such as ultrahigh strength of pentagonal graphene[1], room-temperature quantum spin Hall effect of pentagonal SnX_2 (X = S, Se, Te)[12], magnetic Dirac fermions of pentagonal MoS_2 (ref. 13) and ferromagnetism of semiconducting pentagonal VTe_2 (ref. 14), indicating that pentagonal

---

[1]Department of Physics and Astronomy, Purdue University, West Lafayette, IN, USA. [2]Birck Nanotechnology Center, Purdue University, West Lafayette, IN, USA. [3]Department of Physics and Astronomy and Villum Center for Hybrid Quantum Materials and Devices, Aarhus University, Aarhus, Denmark. [4]Institute of Functional Nano and Soft Materials, Soochow University, Suzhou, China. [5]Department of Physics and Astronomy and Villum Center for Dirac Materials, Aarhus University, Aarhus, Denmark. [6]Center for Nanophase Materials Sciences, Oak Ridge National Laboratory, Oak Ridge, TN, USA. [7]Department of Physics and Astronomy and Center for Storage Ring Facilities (ISA), Aarhus University, Aarhus, Denmark. [8]Purdue Quantum Science and Engineering Institute and School of Electrical and Computer Engineering, Purdue University, West Lafayette, IN, USA. [9]These authors contributed equally: Lina Liu, Yujin Ji. ✉e-mail: dzemlian@purdue.edu; yyli@suda.edu.cn; yongchen@purdue.edu

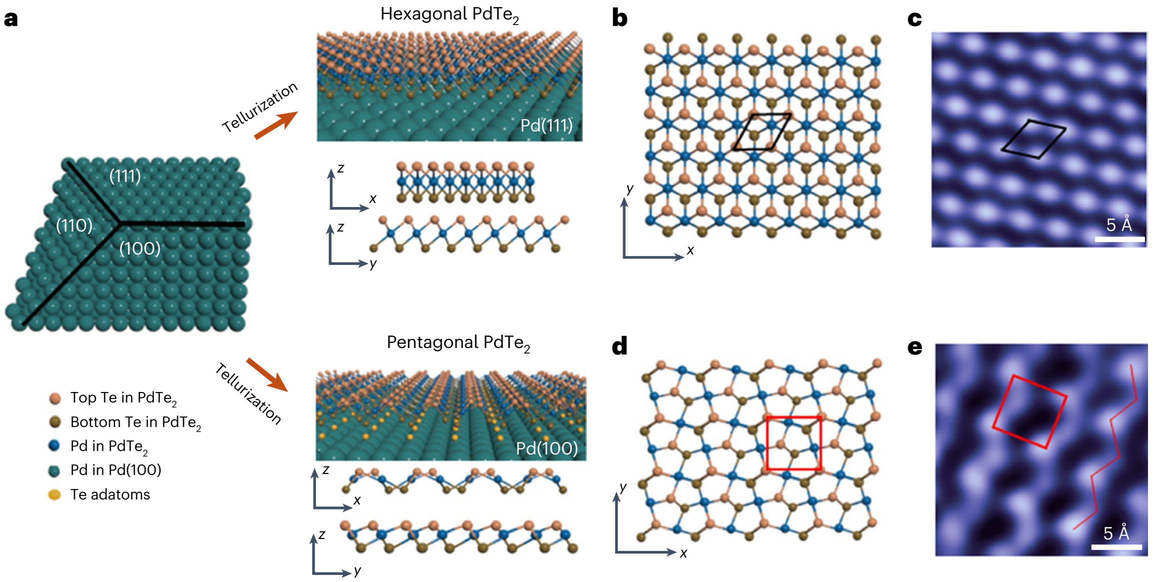

Fig. 1 | Synthesis of monolayer hexagonal and pentagonal $PdTe_2$. a, Schematics of epitaxial growth of monolayer hexagonal and pentagonal $PdTe_2$ by direct tellurization of Pd(111) and Pd(100) surfaces, respectively. This schematic image is to demonstrate key aspects of the growth method only. Tellurium adatoms in the schematic image of pentagonal $PdTe_2$ on Pd(100) are discussed later in the text. **b**,**c**, A schematic lattice image (top view) (**b**) and an atomically resolved STM image of monolayer hexagonal $PdTe_2$ (**c**). **d**,**e**, A schematic lattice image (top view) (**d**) and an atomically resolved STM image of monolayer pentagonal $PdTe_2$ (**e**). Corresponding side views of the lattices shown in **b** and **d** are shown in **a**. Measurement parameters: sample bias voltage $V_b = 0.8$ V, tunnelling current magnitude $I_t = 0.7$ nA for **c** and $V_b = -0.5$ V, $I_t = 0.5$ nA for **e**. Black rhombuses and red squares represent unit cells of hexagonal and pentagonal $PdTe_2$, respectively. Red lines in **e** indicate zigzag chains formed by the topmost tellurium atoms.

2D materials are not only promising materials for novel applications but also demonstrate great potential in fundamental studies of new quantum states and phenomena.

Although pentagonal 2D materials have been theoretically predicted for years, few of them have been studied experimentally[3]. Only recently have $PdSe_2$ and the analogous PdPSe and PdPS, which have pentagonal structures as thermodynamically stable phases, begun to be investigated[15–18] (it should be noted that the bulk crystals of these materials, which have orthorhombic structures, were studied much earlier[19,20]). Their properties, including high mobility and large in-plane anisotropy, have been unveiled, facilitating their applications in functional nanoelectronics[15–18]. In addition, giant non-linear optical activity has been observed in $PdSe_2$ (refs. 21,22), suggesting its potential in optoelectronics. More interestingly, the pentagonal structure offers $PdSe_2$ great flexibilities for structural reconstruction, which provides opportunities for phase engineering[23] and enables interlayer manipulation[24]. However, in contrast to $PdSe_2$, many pentagon-based 2D materials are metastable[25] (Supplementary Fig. 1), which makes the direct synthesis of these materials more challenging. Although previously some metastable phases of hexagon-based 2D TMDCs (such as 1T and 1T′ phases of MoS_2) have been synthesized[26–28], the direct synthesis of pentagon-based metastable phases has never been demonstrated. The lack of proper ways to synthesize and stabilize pentagonal 2D materials (particularly metastable ones) has largely hindered the exploration of this unique class of 2D materials.

We report here the direct synthesis of metastable monolayer pentagonal $PdTe_2$. All the $PdTe_2$ phases so far synthesized (both bulk and 2D layers) demonstrate hexagonal 1T structures[29–31] because the hexagonal phase is energetically favoured by having the lowest formation energy[32]. Based on our density functional theory (DFT) calculations, the formation energy for monolayer pentagonal $PdTe_2$ is only 0.04 eV per atom higher than that of the monolayer hexagonal $PdTe_2$ (Supplementary Fig. 1), suggesting the potential feasibility of synthesizing the pentagonal phase. Here, we use epitaxial growth, which is an efficient way to grow high-quality 2D materials[33,34], for the synthesis of pentagonal $PdTe_2$. During epitaxy, the substrate symmetry plays a crucial role and the as-grown structure can be well controlled and stabilized due to lattice match with the substrate[35]. We demonstrated the synthesis of monolayer pentagonal $PdTe_2$ by symmetry-driven epitaxy through direct tellurization of the Pd(100) surface, the lattice of which exhibits a good match with the lattice of pentagonal $PdTe_2$. The successful growth of monolayer pentagonal $PdTe_2$ was confirmed by various structural and spectroscopic characterizations. Comprehensive scanning tunnelling microscopy (STM) measurements and simulations, combined with low-electron-energy diffraction (LEED) analysis proved the atomic structures of pentagonal $PdTe_2$. X-ray photoelectron spectroscopy (XPS) measurements verified the formation of $PdTe_2$ and the monolayer thickness. Phonon dispersions were revealed by DFT calculations and corresponding lattice vibrational modes were observed by high-resolution electron energy loss spectroscopy (HREELS). The DFT calculations revealed that the monolayer pentagonal $PdTe_2$ is a semiconductor with an indirect bandgap of 1.05 eV, which is consistent with the scanning tunnelling spectroscopy (STS) result. Meanwhile, the valence bands of the monolayer pentagonal $PdTe_2$ were measured by angle-resolved photoemission spectroscopy (ARPES). This direct synthesis, along with the comprehensive measurements of atomic structures, phonon dispersions and electronic structures of monolayer pentagonal $PdTe_2$, will greatly accelerate the research field of pentagonal 2D materials.

We selected different facets of palladium single crystals as substrates for the epitaxial growth of different phases of $PdTe_2$. By taking advantage of the symmetries of the underlying substrates, hexagonal and pentagonal monolayer $PdTe_2$ were successfully synthesized through direct tellurization of Pd(111) and Pd(100) surfaces, respectively (Fig. 1a). The as-grown hexagonal monolayer $PdTe_2$ exhibits a conventional 1T structure (Fig. 1b,c) with $(\sqrt{3} \times \sqrt{3})$ R30° atomic arrangements, which has been discussed in depth in our previous work[36].

In this work, we focus on the pentagonal phase of $PdTe_2$ grown on Pd(100). Before growth, the surface of Pd(100) was freshly cleaned by repeated sputtering and annealing in an ultrahigh vacuum (UHV).

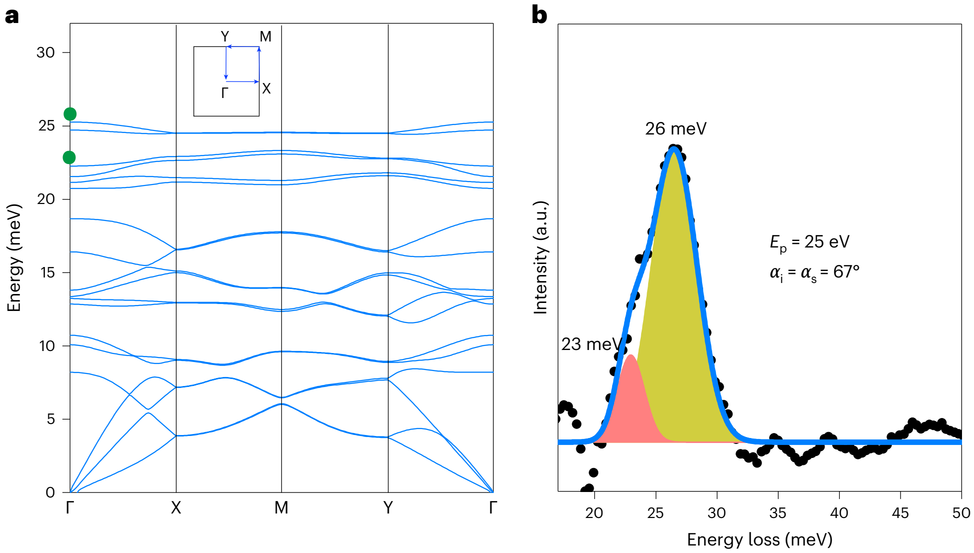

Fig. 2 | Phonons of monolayer pentagonal PdTe$_2$. a, Calculated phonon dispersions of monolayer pentagonal PdTe$_2$ along the Γ–X–M–Y–Γ path of the Brillouin zone as shown in the inset. **b**, An electron-energy-loss spectrum of as-grown pentagonal PdTe$_2$ at the Γ point. The dotted black and solid blue curves are the original data curve (after background subtraction) and the fitting curve, respectively. Red and yellow peaks (at 23 meV and 26 meV, respectively) are the fitting components and their energies are marked as green dots in **a**. The primary electron beam energy (E_p) is 25 eV. The incident and scattering angles (α_i and α_s, respectively) are 67°.

After cleaning, palladium atoms on the surface were full of dangling bonds and chemically reactive. Tellurium was then deposited on the Pd(100) substrate. Annealing at 500 °C induced the formation of pentagonal PdTe$_2$, which as shown below exhibits lattice matching with the Pd(100) substrate (see Supplementary Fig. 2 for details of the growth). This lattice matching serves as the driving force for the growth of the pentagonal phase of PdTe$_2$. Pentagonal PdTe$_2$ presents low crystallographic symmetry with the monoclinic space group[8] $P2_1/c$, which is considerably different from hexagonal PdTe$_2$ which has the high-symmetry space group[37] $P\bar{3}m1$. Its out-of-plane geometries are puckered (Fig. 1a) and its projected in-plane atomic arrangements demonstrate pentagons as the building blocks (Fig. 1d). The projected in-plane structure exhibits a rectangular unit cell (Fig. 1d), with tetra-coordinated[5,15] palladium atoms (where each palladium atom bonds with four tellurium atoms, two from the top and two from the bottom). For the out-of-plane structure, each top tellurium atom pairs with a bottom tellurium atom to form a Te–Te dimer across the layer[5], resulting in a puckered layer with a shorter vertical height of 1.69 Å compared with that (2.76 Å) of the monolayer hexagonal PdTe$_2$[11]. The atomic-resolution STM image taken after growth reveals 1D zigzag chains formed by bright dots (Fig. 1e), indicating low-symmetry arrangements of surface atoms. This structure agrees well with the patterns of the topmost tellurium atoms of pentagonal PdTe$_2$. The measured unit cell of the as-grown structure is square (6.2 Å × 6.2 Å), which is slightly different from the previously calculated rectangular lattice for the free-standing monolayer pentagonal PdTe$_2$, which has a unit cell of 6.1 Å × 6.4 Å (refs. 8,11). The reason for this difference can be ascribed to lattice confinement by the underlying Pd(100) substrate, which has a square lattice. We note that, unlike the Pd(100) lattice, the as-grown PdTe$_2$ lattice is not invariant upon 90° rotation even though it has a square unit cell. According to the Pd–Te phase diagram[38] and a theoretical database of 2D materials[39,40], for all known Pd–Te compounds, the pentagonal PdTe$_2$ we discuss here (β pentagonal phase[3]) is the only one that has a rectangular unit cell with lattice constants close to 6.2 Å × 6.2 Å, consistent with our STM images. Although other types of pentagon-based phases have also been predicted for some materials (such as γ phase for PdS$_2$)[3,41], the β pentagonal phase we discuss here is the only one in which zigzag chains can be formed by the topmost atoms, again consistent with our STM observations, thus confirming our structural assignment. We also note that the as-grown monolayer pentagonal PdTe$_2$ is stable after air exposure (Supplementary Fig. 3), facilitating its potential applications in ambient conditions.

We carried out synchrotron-based XPS measurements to verify the formation of PdTe$_2$. We observed two sets of peaks in the Pd 3d spectra: one set presents lower binding energies of 335.1 eV and 340.4 eV; the other presents higher binding energies of 336.0 eV and 341.3 eV (Supplementary Fig. 4a). The sets of lower and higher binding energies can be attributed to bulk palladium substrate and pentagonal PdTe$_2$, respectively. Two sets of Te 4d peaks were also observed in the XPS spectra (Supplementary Fig. 4b). The lower binding energies of 40.6 eV and 42.1 eV are ascribed to tellurium in PdTe$_2$. The existence of the set of higher binding energies of 41.5 eV and 43.0 eV indicates that there is another type of tellurium in the system. We attribute these higher binding energies to a tellurium adatom layer between the as-grown pentagonal PdTe$_2$ and the Pd(100) substrate, a hypothesis supported by previous works in similar systems (for example, TMDC monolayers epitaxially grown on corresponding single crystals)[42,43] and our DFT calculations. (A comparison between the XPS spectra of as-grown pentagonal and hexagonal PdTe$_2$ demonstrates that tellurium adatoms are unique in pentagonal PdTe$_2$/Pd(100) (Supplementary Fig. 4c). More discussions about tellurium adatoms can be found in Supplementary Figs. 5 and 6 and Supplementary Table 1). Moreover, we carried out the XPS measurements under both normal and grazing emission angles to determine the relative contribution of PdTe$_2$, tellurium adatoms and the Pd(100) substrate (Supplementary Fig. 4a,b). The results show the palladium peak area ratio of PdTe$_2$ to bulk palladium substrate became bigger with grazing emission, whereas the tellurium peak area ratio of tellurium adatoms to PdTe$_2$ became smaller, suggesting that PdTe$_2$ is on top of Pd(100), and the tellurium adatoms are under PdTe$_2$. Based on our XPS results, the thickness of the as-grown pentagonal PdTe$_2$ is estimated[36,44] to be ~1.6 Å, consistent with monolayer pentagonal PdTe$_2$ (ref. 11). This value is also much smaller than the calculated thickness of bilayer pentagonal PdTe$_2$ (5.1 Å), indicating that the as-grown PdTe$_2$ is unlikely to be a bilayer.

In addition, we performed DFT calculations and HREELS measurements to explore the lattice dynamics of monolayer pentagonal PdTe$_2$.

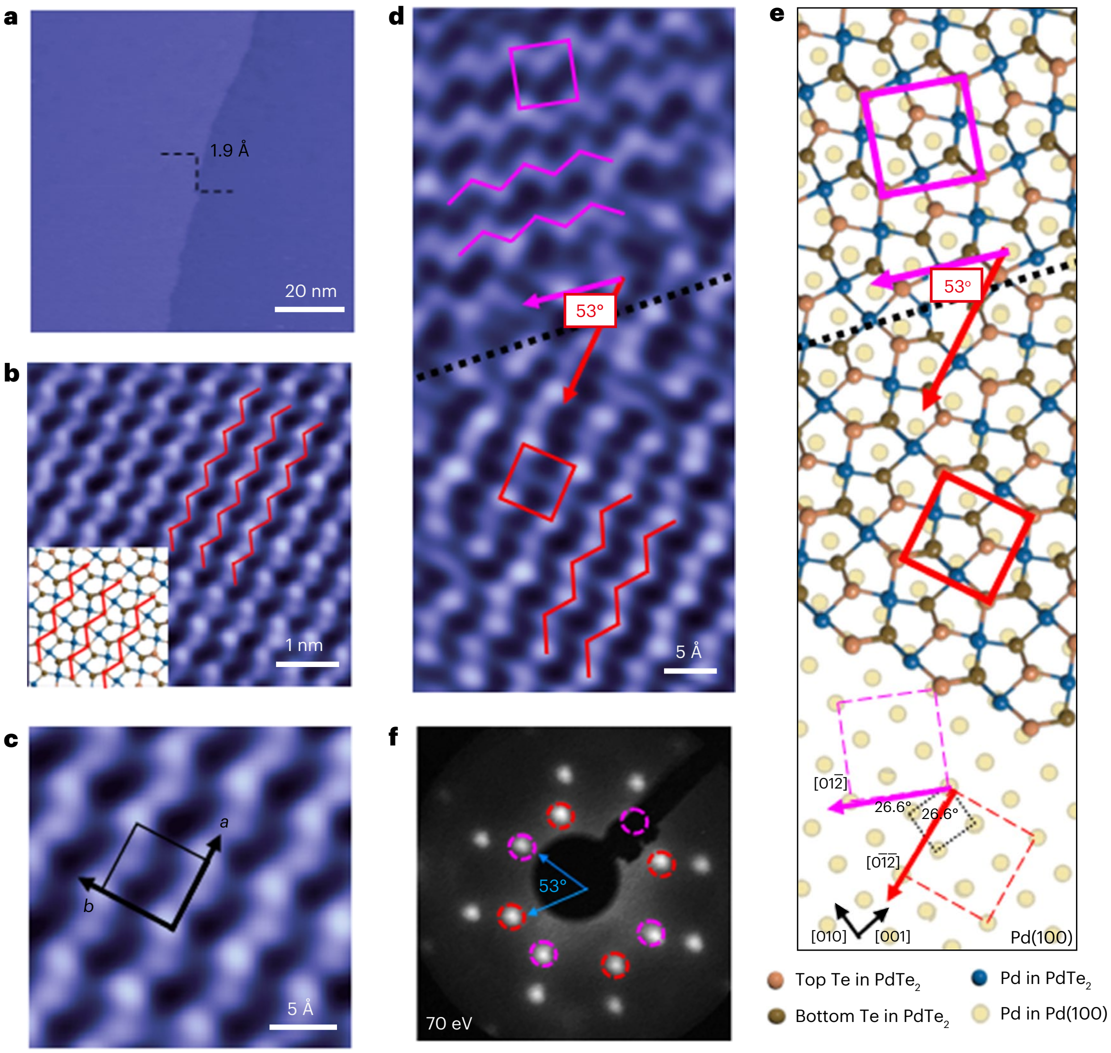

Fig. 3 | STM and LEED measurements of the as-grown monolayer pentagonal PdTe$_2$. **a**–**c**, Topographic (**a**), magnified (**b**) and atomic-resolution (**c**) STM images of the as-grown pentagonal PdTe$_2$. $V_b = 1.0$ V, $I_t = 0.5$ nA for **a**; $V_b = -0.5$ V, $I_t = 0.5$ nA for **b** and **c**. Inset, **b**: a schematic image of pentagonal PdTe$_2$. Red solid lines in **b** represent the zigzag chains formed by tellurium atoms from the topmost layer. The black square in **c** represents the unit cell of pentagonal PdTe$_2$. The direction along zigzag chains is the *a* axis. **d**, An STM image of the as-grown pentagonal PdTe$_2$ showing two crystallographic orientations. $V_b = -0.5$ V, $I_t = 0.5$ nA. The pink and red solid lines represent the zigzag chains formed by tellurium atoms on the topmost layer. **e**, A schematic image showing the *a* axes of the pentagonal PdTe$_2$ lattices grown along the $[01\bar{2}]$ and $[0\bar{1}\bar{2}]$ directions of the Pd(100) topmost surface, demonstrating the stacking geometry and epitaxial relationship. The dashed black square represents the unit cell of the topmost atoms of Pd(100). Black arrows (lower left) indicate the main crystallographic directions of Pd(100). The red and pink squares (solid and dashed) in **d** and **e** represent the unit cells of pentagonal PdTe$_2$ in two orientations. Pink and red arrows in **d** and **e** represent two crystallographic orientations of *a* axes (the direction along the zigzag chains) of the as-grown pentagonal PdTe$_2$. Each orientation has a rotation angle of 26.6° with respect to the unit cell of the topmost atoms of Pd(100). The black dashed lines in **d** and **e** indicate the grain boundary. Note that tellurium adatoms are invisible in **e** because they are covered by the bottom tellurium atoms of PdTe$_2$. **f**, LEED patterns of the as-grown pentagonal PdTe$_2$ measured with a beam energy of 70 eV. Pink and red dashed circles represent the two sets of diffraction patterns. Bright dots without circles are the second-order diffraction patterns. LEED patterns from Pd(100) are not observable in this measurement but were measured separately on a bare Pd(100) substrate without changing the crystal orientation (Supplementary Fig. 10).

The calculated phonon dispersions of monolayer pentagonal PdTe$_2$ (Fig. 2a) show dramatically different features from those of monolayer hexagonal PdTe$_2$ (Supplementary Fig. 7a). HREELS was also utilized to experimentally probe the phonon modes. Two components could be resolved at 23 meV and 26 meV in the energy-loss spectrum measured at the Γ point (Fig. 2b), in reasonable agreement with the calculated optical phonon modes of monolayer pentagonal PdTe$_2$ but notably different from the measured HREELS spectrum (which shows peaks at 15 meV and 25 meV) in monolayer hexagonal PdTe$_2$ (Supplementary Fig. 7b). No modes were observed on the Pd(100) substrate in the same energy region (Supplementary Fig. 8), proving the observed energy-loss modes are from the as-grown pentagonal PdTe$_2$.

To gain a comprehensive understanding of the atomic structures, the as-grown pentagonal PdTe$_2$ was studied by STM and LEED. After growth, the surface as seen by STM is clean and flat over a large area with sometimes an apparent step height of ~1.9 Å (Fig. 3a), consistent with a monoatomic step terrace of Pd(100) and indicating that the monolayer PdTe$_2$ is epitaxially grown on the terrace. Note that all the terraces we observed by STM exhibit a vertical height around this value, consistent with the imaged Pd(100) surface being fully covered by monolayer PdTe$_2$ with no bilayer or multilayer regions found. The magnified STM image shows clear and parallel zigzag chains, implying the as-grown pentagonal PdTe$_2$ has a well-ordered structure and is of high quality (Fig. 3b). Individual atoms were clearly resolved in the zoomed-in STM image

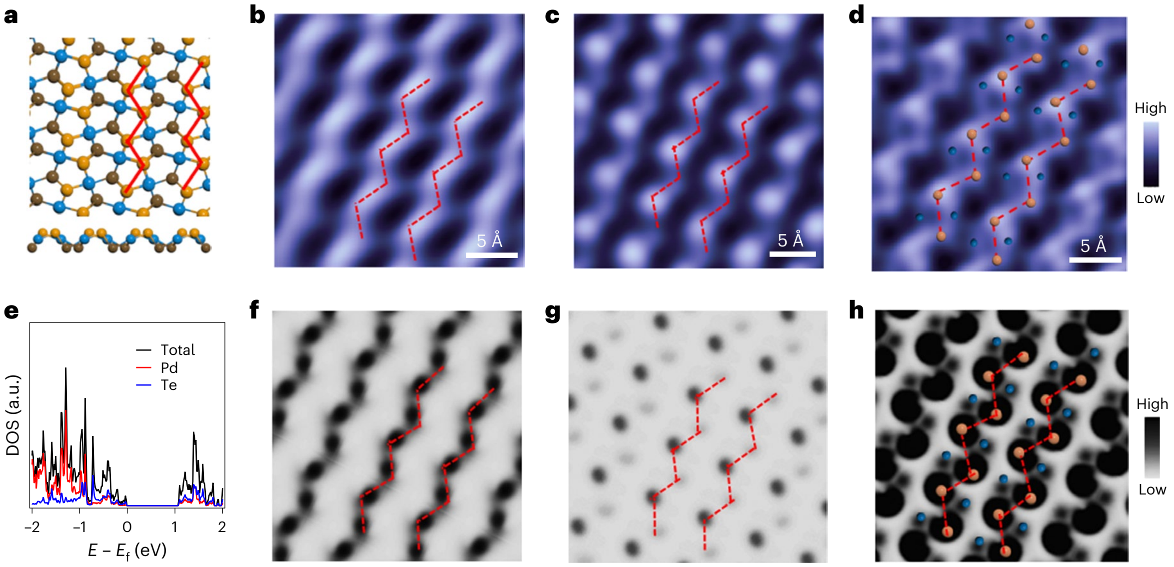

Fig. 4 | Experimental and simulated STM images at various bias voltages. **a**, Schematic images of monolayer pentagonal $PdTe_2$ in top view (upper) and side view (lower). Orange, blue and brown spheres represent top tellurium, palladium and bottom tellurium atoms, respectively. **b**–**d**, Experimental STM images of the as-grown pentagonal $PdTe_2$ at biases of 1.0 V (**b**), −0.5 V (**c**) and −1.0 V (**d**). $I_t = 0.5$ nA. **e**, The calculated DOS for monolayer pentagonal $PdTe_2$. $E - E_f$ represents the electronic energy (E) relative to the Fermi level (E_f). The black curve is the total DOS. The red and blue curves are partial contributions from palladium and tellurium atoms, respectively. **f**–**h**, Simulated STM images at biases of 1.0 V (**f**), −0.5 V (**g**) and −1.0 V (**h**). Red lines (solid and dashed) in all images indicate the zigzag chains formed by tellurium atoms from the topmost layer. Orange and blue dots in **d** and **h** indicate the tellurium atoms on the topmost layer and palladium atoms on the middle layer in the $PdTe_2$, respectively. Note the experimental and simulated STM images have opposite colour scales.

(Fig. 3c), confirming the low-symmetry atomic arrangements of the monolayer pentagonal $PdTe_2$. The unit cell of pentagonal $PdTe_2$ is square with dimensions of 6.2 Å × 6.2 Å, corresponding to the $(\sqrt{5} \times \sqrt{5})$ R26.6° supercell of the underlying Pd(100) ($\sqrt{5} \times 2.75 = 6.15 \approx 6.2$ Å, where the lattice constant of the surface atoms of Pd(100) is 2.75 Å). Notably, even with a square unit cell, the as-grown pentagonal $PdTe_2$ exhibits only a two-fold (180°) rotational symmetry rather than four-fold (90°) rotational symmetry of the square lattice of the underlying Pd(100). Occasionally, coexistence of two differently orientated domains in the as-grown pentagonal $PdTe_2$ could be observed (Fig. 3d). The angle between the two orientations is ~53° (approximately twice 26.6°), indicating that each orientation is rotated symmetrically by ~26.6° with respect to the lattice orientation of Pd(100). The *a* axes (the direction along the zigzag chains) of the two orientations are along the $[01\bar{2}]$ and $[0\bar{1}\bar{2}]$ crystallographic directions of the Pd(100) topmost surface, respectively, illustrating a good epitaxy (Fig. 3e). The lack of four-fold (90°) rotational symmetry means that two other possible orientations for the as-grown pentagonal $PdTe_2$ lattices could also exist by rotating the two observed orientations (Fig. 3d) by 90° (the two other possible lattice vectors are along the $[0\bar{2}\bar{1}]$ and $[0\bar{2}1]$ directions as shown in Supplementary Fig. 9, although we have not yet observed $PdTe_2$ domains along these two directions, possibly due to the small STM scanning areas). Furthermore, LEED characterizations were carried out to examine the crystallinity and orientation of the as-grown pentagonal $PdTe_2$ on a millimetre scale. As shown in Fig. 3f, bright and sharp diffraction spots were observed, proving the high crystallinity of the as-grown pentagonal $PdTe_2$ layer over a large surface area. Two sets of diffraction patterns with a rotation angle of ~53° between them were clearly identified, which is consistent with the rotation angle between the two domains observed by STM (Fig. 3d). Comparing the LEED patterns of pentagonal $PdTe_2$ with those of bare Pd(100) (Supplementary Fig. 10) further confirms that each set of $PdTe_2$ diffraction patterns is rotated by ~26.6° with respect to the diffraction pattern (lattice orientation) of Pd(100). It should be noted that the LEED patterns obtained on the pentagonal $PdTe_2$ possess a four-fold (90°) rotational symmetry and thus it is not possible to distinguish two orientations that are rotated by 90° from each other (in other words, the observed LEED patterns could be consistent with two, three or four different orientations coexisting on the surface measured).

We carried out further STM measurements and theoretical simulations under various tunnelling voltages to explore the topographic structures of the pentagonal $PdTe_2$ and the electronic effects. Atomically resolved STM images of pentagonal $PdTe_2$ exhibit a strong dependence on tunnelling biases (Fig. 4), similar to that of bulk $PdSe_2$ (ref. 45). At tunnelling biases of 1.0 V and −0.5 V, only features of the zigzag chains formed by the topmost tellurium atoms were resolved (Fig. 4b,c). At a large negative tunnelling bias of −1.0 V, signals from palladium atoms in the middle layer of $PdTe_2$ became visible (Fig. 4d). This observed bias dependence could be explained by the calculated total density of states (DOS) (Fig. 4e): palladium atoms are found to contribute much more strongly to the DOS at more negative energies (relative to the Fermi level). Therefore, the STM image collected at −1.0 V reveals the combination of topographic and electronic effects, whereas at positive and small negative energies, the topographic effect is dominant. The simulated STM images at different biases (Fig. 4f–h) are in agreement with the corresponding experimental STM images, confirming the high quality of the as-grown monolayer pentagonal $PdTe_2$.

To further understand the electronic structures, we performed DFT calculations for the electron band structures of monolayer pentagonal $PdTe_2$. The valence band maximum (VBM) of monolayer pentagonal $PdTe_2$ is along the Γ–X path (defined as along the zigzag chain direction in our calculation) while the conduction band minimum (CBM) is along the Γ–Y path (perpendicular to the zigzag chain direction), leading to an indirect bandgap of 1.05 eV (Fig. 5a and Supplementary Fig. 11), which is dramatically different from the narrow indirect bandgap of monolayer hexagonal $PdTe_2$ of 0.33 eV (Supplementary Fig. 12). Valence band structures along three high-symmetry directions, Y–Γ–Y, X–Γ–X and M–Γ–M, were plotted and valence bands dispersed in a 'M shape' were observed in all three directions near the Fermi level (Supplementary Fig. 13). The calculated value of the bandgap and main features of the band structures are comparable with previous

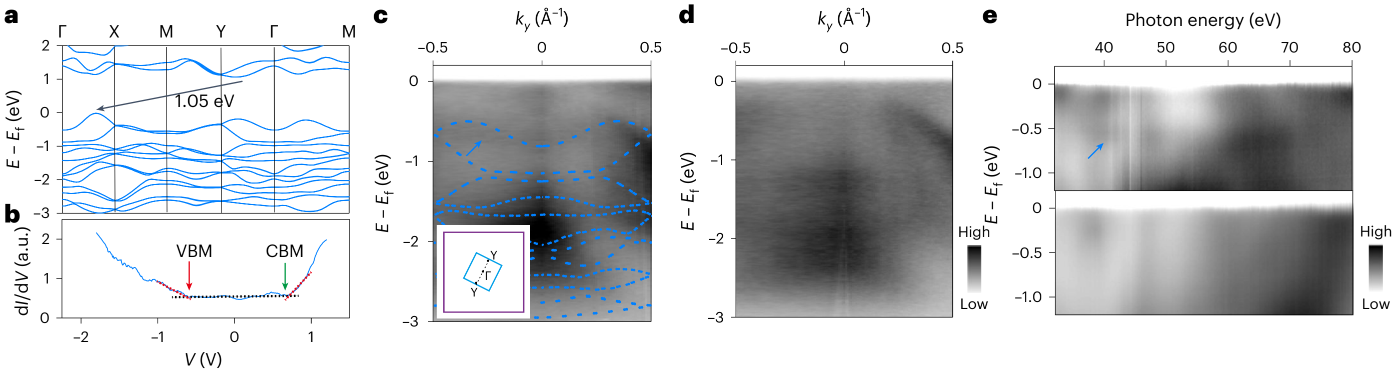

Fig. 5 | Band structures of monolayer pentagonal $PdTe_2$. a, Calculated band structures of monolayer pentagonal $PdTe_2$ with spin–orbital coupling. **b**, An STS spectrum of monolayer pentagonal $PdTe_2$ on Pd(100). $V_b = -100$ mV, $I_t = 50$ pA. The ~1.2 eV bandgap is obtained by measuring the intersections of sharp rises (red dashed lines) and the baseline value of the conductance (black dashed line). Red and green arrows indicate the intersections, corresponding to energies near the VBM and CBM, respectively. **c**, Overall ARPES results of monolayer pentagonal $PdTe_2$ extracted along the Y–Γ–Y direction (defined for one domain orientation relative to the substrate Brillouin zone as indicated in the inset). The blue arrow points to the 'M-shaped' valence band. The calculated band structures along the Y–Γ–Y direction are superimposed with blue dashed lines. The ARPES result without superimposed calculated band structures is shown in Supplementary Fig. 17. Inset: Brillouin zones of one pentagonal $PdTe_2$ domain (blue square) and underlying Pd(100) substrate (larger purple square). **d**, ARPES result of clean Pd(100) substrate extracted along the same direction as that in **c**. **e**, Photon-energy-dependent spectra at the Γ points for pentagonal $PdTe_2$ (upper panel) and clean Pd(100) (lower panel). The blue arrow points to the non-dispersion pentagonal $PdTe_2$-related band.

calculated results[8,10,11]. To confirm the semiconducting nature and probe the bandgap, we performed STS measurements. The STS curve of the as-grown monolayer pentagonal $PdTe_2$ shows a suppressed conductance region with two onsets of ~−0.6 V and ~0.6 V, leading to an estimated bandgap of ~1.2 eV (Fig. 5b). This is in reasonable agreement with the calculated 1.05 eV bandgap of monolayer pentagonal $PdTe_2$ (noting that DFT calculations are known to underestimate the bandgap[46,47] and were performed on free-standing pentagonal $PdTe_2$). Meanwhile the ~1.2 eV bandgap is much bigger than the calculated 0.39 eV bandgap for bilayer and the zero bandgap for trilayer pentagonal $PdTe_2$ (Supplementary Fig. 14), further suggesting that the as-grown $PdTe_2$ is monolayer. The small non-zero conductance within the bandgap in the STS curve could be attributed to the tunnelling to the palladium substrate, as commonly observed in STS curves of monolayer 2D semiconducting materials on metallic substrates[48,49]. We also conducted ARPES measurements to further probe the band structures of monolayer pentagonal $PdTe_2$ (note that only valence bands were measured because the conduction bands lie above the Fermi level). ARPES results of the as-grown $PdTe_2$ and clean Pd(100) substrate extracted along the Y–Γ–Y direction (Fig. 5c, inset) are shown in Fig. 5c,d, respectively. Because domains of four orientations of pentagonal $PdTe_2$ could be present simultaneously on the surface, band dispersion cutting from the Γ–Y direction of one orientation domain could be superimposed with contributions from domains of other possible orientations, approximately in the Γ–M and Γ–X directions (Supplementary Fig. 15). Given the similarity of the dispersion in the Γ–Y, Γ–M and Γ–X directions (Supplementary Fig. 13), this would merely result in a broadened band of the 'M-shaped' valence band. The observed 'M-shaped' dispersing band located at ~−0.65 eV at the Γ point is thus consistent with the calculated valence band structures. This 'M-shaped' band was also observed along the Γ–X direction (Supplementary Fig. 16). In addition to the broadening by the simultaneous presence of differently orientated domains, the $PdTe_2$ bands are likely to experience additional broadening and change of dispersion due to the interaction with the substrate. On the other hand, the 'M-shaped' band clearly retains a 2D character because it does not disperse with different photon energies (Fig. 5e), suggesting the 2D nature of the monolayer pentagonal $PdTe_2$.

In conclusion, we demonstrated the tellurization-based direct synthesis of metastable monolayer pentagonal $PdTe_2$ driven by symmetry epitaxy and provided comprehensive characterizations on this pentagonal 2D material. As confirmed by STM and LEED, the as-grown pentagonal $PdTe_2$ exhibited one-dimensional zigzag atomic chains, with the unit cell matching the $(\sqrt{5}\times\sqrt{5})$ R26.6° supercell of the underlying Pd(100) substrate. XPS verified the formation of $PdTe_2$ and suggested its monolayer thickness. We used HREELS to probe the lattice vibrations of $PdTe_2$ and the spectra experimentally obtained were consistent with the calculated phonon modes of monolayer pentagonal $PdTe_2$. The experimental STM images of monolayer pentagonal $PdTe_2$ at various bias voltages showed strong bias dependence, which is also clearly revealed in the simulated STM images. Calculated band structures demonstrated that monolayer pentagonal $PdTe_2$ is a semiconductor with an indirect bandgap of 1.05 eV, which agrees with the STS-measured bandgap. The valence band structures were further measured by ARPES, which revealed features consistent with the calculations. Symmetry-driven epitaxial growth provides a viable route for the synthesis of pentagon-based 2D materials, even for metastable phases. Our method will add this unique group of materials to the 2D materials family, which has so far been dominated by hexagon-based phases, and expand it to include a large number of low-symmetry members. This will also bring unprecedented opportunities for 2D materials in applications such as functional electronics based on in-plane anisotropy, optoelectronics originating from non-linear light–matter interaction and thermoelectric devices benefiting from the low thermal conductivity.

Online content

Any methods, additional references, Nature Portfolio reporting summaries, source data, extended data, supplementary information, acknowledgements, peer review information; details of author contributions and competing interests; and statements of data and code availability are available at https://doi.org/10.1038/s41563-024-01987-w.

References

1. Zhang, S. et al. Penta-graphene: a new carbon allotrope. *Proc. Natl Acad. Sci. USA* **112**, 2372–2377 (2015).
2. Wang, Y., Li, Y. & Chen, Z. Not your familiar two-dimensional transition metal disulfide: structural and electronic properties of the PdS_2 monolayer. *J. Mater. Chem. C* **3**, 9603–9608 (2015).
3. Shen, Y. & Wang, Q. Pentagon-based 2D materials: classification, properties and applications. *Phys. Rep.* **964**, 1–42 (2022).

4. Liang, Q. J., Chen, Z. L., Zhang, Q. & Wee, A. T. S. Pentagonal 2D transition metal dichalcogenides: $PdSe_2$ and beyond. *Adv. Funct. Mater.* **32**, 2203555 (2022).
5. Kempt, R., Kuc, A. & Heine, T. Two-dimensional noble-metal chalcogenides and phosphochalcogenides. *Angew. Chem. Int. Ed.* **59**, 9242–9254 (2020).
6. Gu, Y. et al. Two-dimensional palladium diselenide with strong in-plane optical anisotropy and high mobility grown by chemical vapor deposition. *Adv. Mater.* **32**, e1906238 (2020).
7. Jiang, S. et al. Anisotropic growth and scanning tunneling microscopy identification of ultrathin even-layered $PdSe_2$ ribbons. *Small* **15**, e1902789 (2019).
8. Lan, Y.-S., Chen, X.-R., Hu, C.-E., Cheng, Y. & Chen, Q.-F. Penta-PdX_2 (X=S, Se, Te) monolayers: promising anisotropic thermoelectric materials. *J. Mater. Chem. A* **7**, 11134–11142 (2019).
9. Tao, W. L., Zhao, Y. Q., Zeng, Z. Y., Chen, X. R. & Geng, H. Y. Anisotropic thermoelectric materials: pentagonal PtM_2 (M=S, Se, Te). *ACS Appl. Mater. Interfaces* **13**, 8700–8709 (2021).
10. Marfoua, B. & Hong, J. High thermoelectric performance in hexagonal 2D $PdTe_2$ monolayer at room temperature. *ACS Appl. Mater. Interfaces* **11**, 38819–38827 (2019).
11. Xiong, W., Huang, K. & Yuan, S. The mechanical, electronic and optical properties of two-dimensional transition metal chalcogenides MX_2 and M_2X_3 (M=Ni, Pd; X=S, Se, Te) with hexagonal and orthorhombic structures. *J. Mater. Chem. C* **7**, 13518–13525 (2019).
12. Ma, Y., Kou, L., Li, X., Dai, Y. & Heine, T. Room temperature quantum spin Hall states in two-dimensional crystals composed of pentagonal rings and their quantum wells. *NPG Asia Mater.* **8**, e264 (2016).
13. Li, X. Y., Meng, S. & Sun, J. T. Emergence of *d*-orbital magnetic Dirac fermions in a MoS_2 monolayer with squared pentagon structure. *Phys. Rev. B* **101**, 144409 (2020).
14. Li, X. et al. Monolayer puckered pentagonal VTe_2: an emergent two-dimensional ferromagnetic semiconductor with multiferroic coupling. *Nano Res.* **15**, 1486–1491 (2021).
15. Oyedele, A. D. et al. $PdSe_2$: pentagonal two-dimensional layers with high air stability for electronics. *J. Am. Chem. Soc.* **139**, 14090–14097 (2017).
16. Li, P. et al. Penta-PdPSe: a new 2D pentagonal material with highly in-plane optical, electronic, and optoelectronic anisotropy. *Adv. Mater.* **33**, e2102541 (2021).
17. Chow, W. L. et al. High mobility 2D palladium diselenide field-fffect transistors with tunable ambipolar characteristics. *Adv. Mater.* **29**, 1602969 (2017).
18. Duan, R. et al. 2D Cairo pentagonal PdPS: air-stable anisotropic ternary semiconductor with high optoelectronic performance. *Adv. Funct. Mater.* **32**, 2113255 (2022).
19. Folmer, J. C. W., Turner, J. A. & Parkinson, B. A. Amelioration of the photoresponse of PdPS photoanodes by ferrocyanide electrolytes. *Inorg. Chem.* **24**, 4028–4030 (1985).
20. Folmer, J. C. W., Turner, J. A. & Parkinson, B. A. Photoelectrochemical characterization of several semiconducting compounds of palladium with sulfur and/or phosphorus. *J. Solid State Chem.* **68**, 28–37 (1987).
21. Yu, J. et al. Giant nonlinear optical activity in two-dimensional palladium diselenide. *Nat. Commun.* **12**, 1083 (2021).
22. Jia, L., Wu, J., Yang, T., Jia, B. & Moss, D. J. Large third-order optical Kerr nonlinearity in nanometer-thick $PdSe_2$ 2D dichalcogenide films: implications for nonlinear photonic devices. *ACS Appl. Nano Mater.* **3**, 6876–6883 (2020).
23. Oyedele, A. D. et al. Defect-mediated phase transformation in anisotropic two-dimensional $PdSe_2$ crystals for seamless electrical contacts. *J. Am. Chem. Soc.* **141**, 8928–8936 (2019).
24. Lin, J. et al. Novel Pd_2Se_3: two-dimensional phase driven by interlayer fusion in layered $PdSe_2$. *Phys. Rev. Lett.* **119**, 016101 (2017).
25. Guo, Y. G., Zhou, J., Xie, H. H., Chen, Y. Y. & Wang, Q. Screening transition metal-based polar pentagonal monolayers with large piezoelectricity and shift current. *NPJ Comput. Mater.* **8**, 40 (2022).
26. Fang, Y. et al. Structure re-determination and superconductivity observation of bulk 1T MoS_2. *Angew. Chem. Int. Ed.* **57**, 1232–1235 (2018).
27. Liu, L. et al. Phase-selective synthesis of 1T′ MoS_2 monolayers and heterophase bilayers. *Nat. Mater.* **17**, 1108–1114 (2018).
28. Zhang, Q. et al. Simultaneous synthesis and integration of two-dimensional electronic components. *Nat. Electron.* **2**, 164–170 (2019).
29. D'Olimpio, G. et al. $PdTe_2$ transition-metal dichalcogenide: chemical reactivity, thermal stability, and device implementation. *Adv. Funct. Mater.* **30**, 1906556 (2019).
30. Zheng, J. et al. Chemical synthesis and integration of highly conductive $PdTe_2$ with low-dimensional semiconductors for *p*-type transistors with low contact barriers. *Adv. Mater.* **33**, e2101150 (2021).
31. Liu, C. et al. Two-dimensional superconductivity and topological states in $PdTe_2$ thin films. *Phys. Rev. Mater.* **2**, 094001 (2018).
32. Liu, W. et al. New Verbeekite-type polymorphic phase and rich phase diagram in the $PdSe_{2-x}Te_x$ system. *Phys. Rev. B* **104**, 024507 (2021).
33. Chen, T. A. et al. Wafer-scale single-crystal hexagonal boron nitride monolayers on Cu(111). *Nature* **579**, 219–223 (2020).
34. Li, T. et al. Epitaxial growth of wafer-scale molybdenum disulfide semiconductor single crystals on sapphire. *Nat. Nanotechnol.* **16**, 1201–1207 (2021).
35. Dong, J., Zhang, L., Dai, X. & Ding, F. The epitaxy of 2D materials growth. *Nat. Commun.* **11**, 5862 (2020).
36. Liu, L., Zemlyanov, D. & Chen, Y. P. Epitaxial growth of monolayer $PdTe_2$ and patterned $PtTe_2$ by direct tellurization of Pd and Pt surfaces. *2D Mater.* **8**, 045033 (2021).
37. Li, E. et al. High quality $PdTe_2$ thin films grown by molecular beam epitaxy. *Chin. Phys. B* **27**, 5 (2018).
38. Okamoto, H. The Pd–Te system (palladium–tellurium). *J. Phase Equilibria* **13**, 73–78 (1992).
39. Gjerding, M. N. et al. Recent progress of the computational 2D materials database (C2DB). *2D Mater.* **8**, 044002 (2021).
40. Haastrup, S. et al. The computational 2D materials database: high-throughput modeling and discovery of atomically thin crystals. *2D Mater.* **5**, 042002 (2018).
41. Zhang, W., Cui, Y., Zhu, C., Huang, B. & Yan, S. Flexible ferroelasticity in monolayer PdS_2: a DFT study. *Phys. Chem. Chem. Phys.* **23**, 10551–10559 (2021).
42. Bosnar, M., Caciuc, V., Atodiresei, N., Lončarić, I. & Blügel, S. Se intercalation between $PtSe_2$ and the Pt surface during synthesis of $PtSe_2$ by direct selenization of Pt(111). *Phys. Rev. B* **102**, 115427 (2020).
43. Perea Acosta, J., Barral, M. A. & Maria Llois, A. Monolayer of $PtSe_2$ on Pt(111): is it metallic or insulating? *J. Phys. Condens. Matter* **32**, 235002 (2020).
44. Zemlyanov, D. Y. et al. Versatile technique for assessing thickness of 2D layered materials by XPS. *Nanotechnology* **29**, 115705 (2018).
45. Fu, M. et al. Defects in highly anisotropic transition-metal dichalcogenide $PdSe_2$. *J. Phys. Chem. Lett.* **11**, 740–746 (2020).
46. Perdew, J. P. & Levy, M. Physical content of the exact Kohn–Sham orbital energies: bandgaps and derivative discontinuities. *Phys. Rev. Lett.* **51**, 1884–1887 (1983).

47. Verma, P. & Truhlar, D. G. HLE16: a local Kohn–Sham gradient approximation with good performance for semiconductor band gaps and molecular excitation energies. *J. Phys. Chem. Lett.* **8**, 380–387 (2017).
48. Sorensen, S. G. et al. Structure and electronic properties of in situ synthesized single-layer MoS_2 on a gold surface. *ACS Nano* **8**, 6788–6796 (2014).
49. Tumino, F., Casari, C. S., Passoni, M., Russo, V. & Li Bassi, A. Pulsed laser deposition of single-layer MoS_2 on Au(111): from nanosized crystals to large-area films. *Nanoscale Adv.* **1**, 643–655 (2019).

Methods

Growth of monolayer pentagonal $PdTe_2$

Epitaxial growth was conducted in an UHV preparation chamber with a base pressure of ~1×10^{-9} mbar. Pd(100) single crystal was used after repeated cycles of Ar^+ sputtering (1 kV, 10 mA for 10 min at an argon background pressure of ~1.0×10^{-6} mbar) and annealing (~700 °C for 20 min) until clear diffraction patterns were observed by LEED. Tellurium (99.999%, Sigma-Aldrich) was thermally evaporated using a home-built evaporator installed in the preparation chamber. The substrate was kept at room temperature during deposition. The source was kept at ~295 °C for 20 min for evaporation. After deposition, annealing was conducted at 500 °C for 20 min for the $PdTe_2$ growth presented in the main text.

Characterizations of as-grown $PdTe_2$

STM, LEED, XPS and HREELS measurements were done at room temperature (unless otherwise noted) in an analysis chamber connected to the preparation chamber with a base pressure of ~8.0×10^{-11} mbar. STM images (Omicron ambient temperature UHV STM) were collected using electrochemically etched tungsten tips at a constant current (topographic) mode (with tips grounded) and were processed using WSxM software. LEED measurements were conducted with a four-grid optics (Omicron LEED). Laboratory-based XPS was acquired using non-monochromatic Mg Kα X-ray radiation ($h\nu = 1{,}253.6$ eV) at 150 W. High-resolution spectra were recorded at a constant pass energy of 20 eV using an Omicron EAC 125 electron energy analyser and an Omicron EAC 2000 analyser controller. XPS results were analysed using CasaXPS. The finite Lorentzian function and the Shirley background function were used for the line shape and background fittings (unless otherwise noted), respectively. HREELS was performed with an ELS5000 (LK Technologies). The primary electron beam energy used in this work was 25 eV. The incident and scattering angles were 67°. STS measurements were carried out at 100 K in a separate Omicron variable temperature STM. Synchrotron-based XPS was collected at the ASTRID2 synchrotron (MatLine) facility at Aarhus University. MatLine is equipped with an SX-700 monochromator and a SPECS PHOIBOS 150 electron energy analyser (http://www.isa.au.dk/). The analyser was operated at a pass energy of 20 eV and had a curved analyser slit of 0.8 mm. The beamline monochromator exit slit was set to a width of 30 μm. Photon energies of 410 eV and 80 eV were used to acquire the Pd 3*d* and Te 4*d* spectra, respectively. ARPES spectra were acquired at the SGM3 beamline[50] at ASTRID2[51], using different photon energies in the range from 20 eV to 130 eV. The data shown in the main text have been acquired using linearly polarized light of 70 eV at 45 K with a combined energy and angle resolution better than 40 meV and 0.2°. The beam spot size on the sample is about 190 μm × 90 μm and is linearly polarized. The monolayer pentagonal $PdTe_2$ and clean Pd(100) in the synchrotron facility were prepared in situ with methods analogous to those presented earlier, with quality and crystallinity cross-checked with a home-built room-temperature Aarhus XPS, STM and LEED to confirm the consistency. Fermi surface mapping obtained by ARPES helped to determine the high-symmetry crystal axes of $PdTe_2$ relative to the Pd(100) substrate.

DFT calculations

All calculations were conducted in the Vienna Ab initio Software Package v.5.4.1 in the framework of DFT with the basis sets of the projector augmented wave[52–55]. We adopted the revised Perdew–Burke–Ernzerhof functional under the Pade approximation[56] for geometry optimization in a primitive cell (detailed information is provided at https://github.com/Austin6035/DFT-characterization-of-PdTe2-on-Pd). We set up a model with tellurium adatoms on the palladium substrate surface (Supplementary Fig. 5b), constituting a buffer layer with tellurium atoms staying on the hollow sites of Pd(100), between Pd(100) and $PdTe_2$. This model was built because our XPS results (Supplementary Fig. 4b) and some previous studies suggested the existence of a buffer layer in similar systems (TMDC monolayers epitaxially grow on corresponding single crystals[42,43]). After structural optimization with the model, all calculated results were based on free-standing monolayer pentagonal $PdTe_2$ with an optimized structure. Band structures were calculated with the Perdew–Burke–Ernzerhof functional. The kinetic cut-off energy was set to 450 eV and the thresholds of total energy and Feynman–Hellman force during structural optimizations were 10^{-4} eV and −0.01 eV Å^{-1}, respectively. Gamma-centred Monkhorst–Pack grids of 4 × 4 × 1 were sampled in the Brillouin zones. A vacuum space of 15 Å was added along the *z* direction to avoid any influence of periodic imaging. Phonon dispersions of monolayer pentagonal and hexagonal $PdTe_2$ were calculated with the local density approximation functional.

Data availability

The source data for the main figures in this study are available via figshare at https://doi.org/10.6084/m9.figshare.22724963 (ref. 57). Other data that support the findings of this work are included in the main text and the Supplementary Information.

References

50. Hoffmann, S., Søndergaard, C., Schultz, C., Li, Z. & Hofmann, P. An undulator-based spherical grating monochromator beamline for angle-resolved photoemission spectroscopy. *Nucl. Instrum. Methods Phys. Res. A* **523**, 441–453 (2004).
51. Bianchi, M. et al. Status and strategy at ISA, Centre for Storage Ring Facilities, Aarhus University, Denmark. *Eur. Phys. J.* **138**, 132 (2023).
52. Hohenberg, P. & Kohn, W. Inhomogeneous electron gas. *Phys. Rev.* **136**, B864–B871 (1964).
53. Blöchl, P. E. Projector augmented-wave method. *Phys. Rev. B* **50**, 17953–17979 (1994).
54. Kresse, G. & Joubert, D. From ultrasoft pseudopotentials to the projector augmented-wave method. *Phys. Rev. B* **59**, 1758–1775 (1999).
55. Kresse, G. & Furthmüller, J. Efficient iterative schemes for *ab* initio total-energy calculations using a plane-wave basis set. *Phys. Rev. B* **54**, 11169–11186 (1996).
56. Hammer, B., Hansen, L. B. & Nørskov, J. K. Improved adsorption energetics within density-functional theory using revised Perdew–Burke–Ernzerhof functionals. *Phys. Rev. B* **59**, 7413–7421 (1999).
57. Liu, L., Ji, Y. & Hus, S. M. A metastable pentagonal 2D material synthesized by symmetry-driven epitaxy. *Figshare* https://doi.org/10.6084/m9.figshare.22724963 (2024).

Acknowledgements

L.L., D.Y.Z. and Y.P.C. acknowledge partial financial support by the US Department of Energy (Office of Basic Energy Sciences) under award number DE-SC0019215 (for synthesis) and Multidisciplinary University Research Initiatives (MURI) Program under award number FA9550-20-1-0322 (for characterizations). Y.J. and Y.L. acknowledge support by the Natural Science Foundation of Jiangsu Province (BK20200873, BZ2020011) and the National Natural Science Foundation of China (grants number 22173067). M.B., J.A.M. and P.H. acknowledge support by VILLUM FONDEN via the Centre of Excellence for Dirac Materials (grant number 11744). L.L., R.B. and Y.P.C. also acknowledge support by VILLUM FONDEN via the Villum Investigator Program (grant number 25931). Part of the STM measurements (at low temperature) were performed in the Center for Nanophase Materials Sciences (CNMS), which is a US Department of Energy, Office of Science User Facility at Oak Ridge National Laboratory. We express our gratitude to the Center for Nanoscale Materials of Argonne National Laboratory and in particular to N. P. Guisinger for the help with the STM tip preparation. We also acknowledge helpful discussions with E. D. Bøjesen, C. Bugge, R. E. Diaz, Y. Ikuhara, L. H. Klausen, T. Koyama, A. Kumatani, K. K. Neelisetty and the team at Thermo Fisher Scientific, Y. Ouyang, M. Saito and J. Smith.

Author contributions

L.L. and D.Y.Z. designed the experiments. L.L. and D.Y.Z. performed the experiments and data analysis. Y.J. and Y.L. performed the DFT calculations. M.B., R.B., J.A.M. and P.H. performed the ARPES measurements and data analysis. S.M.H. and A.-P.L. performed the STS measurements and data analysis. Z.L. worked on the synchrotron-based XPS measurements and data analysis. Y.P.C. coordinated the collaboration and advised the project. L.L. wrote the paper with input from all other coauthors. All authors discussed the results and approved the final version.

Competing interests

The authors declare no competing interests.

Additional information

Supplementary information The online version contains supplementary material available at https://doi.org/10.1038/s41563-024-01987-w.

Correspondence and requests for materials should be addressed to Dmitry Y. Zemlyanov, Youyong Li or Yong P. Chen.

Peer review information *Nature Materials* thanks Thomas Heine, Ki Kang Kim and Kai Xiao for their contribution to the peer review of this work.